First-in-Humans Evaluation of ^{18}F-SMBT-1, a Novel ^{18}F-Labeled Monoamine Oxidase-B PET Tracer for Imaging Reactive Astrogliosis

Victor L. Villemagne[1,2], Ryuichi Harada[3,4], Vincent Doré[2,5], Shozo Furumoto[6], Rachel Mulligan[2], Yukitsuka Kudo[4], Samantha Burnham[5], Natasha Krishnadas[2], Svetlana Bozinovski[2], Kun Huang[2], Brian J. Lopresti[7], Kazuhiko Yanai[3], Christopher C. Rowe[2,8,9], and Nobuyuki Okamura[10]

[1]Department of Psychiatry, University of Pittsburgh, Pittsburgh, Pennsylvania; [2]Department of Molecular Imaging and Therapy, Austin Health, Melbourne, Victoria, Australia; [3]Department of Pharmacology, Tohoku University School of Medicine, Sendai, Japan; [4]Institute of Development of Aging and Cancer, Tohoku University, Sendai, Japan; [5]CSIRO Health and Biosecurity Flagship: Australian e-Health Research Centre, Melbourne, Victoria, Australia; [6]Cyclotron and Radioisotope Center, Tohoku University, Sendai, Japan; [7]Department of Radiology, University of Pittsburgh, Pittsburgh, Pennsylvania; [8]Florey Institute of Neuroscience and Mental Health, University of Melbourne, Melbourne, Victoria, Australia; [9]Australian Dementia Network, Melbourne, Victoria, Australia; and [10]Division of Pharmacology, Faculty of Medicine, Tohoku Medical and Pharmaceutical University, Sendai, Japan

Reactive gliosis, characterized by reactive astrocytes and activated microglia, contributes greatly to neurodegeneration throughout the course of Alzheimer disease (AD). Reactive astrocytes overexpress monoamine oxidase B (MAO-B). We characterized the clinical performance of ^{18}F-(S)-(2-methylpyrid-5-yl)-6-[(3-fluoro-2-hydroxy)propoxy]-quinoline (^{18}F-SMBT-1), a novel MAO-B PET tracer as a potential surrogate marker of reactive astrogliosis. **Methods:** Seventy-seven participants—53 who were elderly and cognitively normal, 7 with mild cognitive impairment, 7 with AD, and 10 who were young and cognitively normal—were recruited for the different aspects of the study. Older participants underwent 3-dimensional magnetization-prepared rapid gradient-echo MRI and amyloid-β, tau, and ^{18}F-SMBT-1 PET. To ascertain ^{18}F-SMBT-1 selectivity to MAO-B, 9 participants underwent 2 ^{18}F-SMBT-1 scans, before and after receiving 5 mg of selegiline twice daily for 5 d. To compare selectivity, ^{18}F-THK5351 studies were also conducted before and after selegiline. Amyloid-β burden was expressed in centiloids. ^{18}F-SMBT-1 outcomes were expressed as SUV, as well as tissue ratios and binding parameters using the subcortical white matter as a reference region. **Results:** ^{18}F-SMBT-1 showed robust entry into the brain and reversible binding kinetics, with high tracer retention in basal ganglia, intermediate retention in cortical regions, and the lowest retention in cerebellum and white matter, which tightly follows the known regional brain distribution of MAO-B ($R^2 = 0.84$). More than 85% of ^{18}F-SMBT-1 signal was blocked by selegiline across the brain, and in contrast to ^{18}F-THK5351, no residual cortical activity was observed after the selegiline regimen, indicating high selectivity for MAO-B and low nonspecific binding. ^{18}F-SMBT-1 also captured the known MAO-B increases with age, with an annual rate of change (~2.6%/y) similar to the in vitro rates of change (~1.9%/y). Quantitative and semiquantitative measures of ^{18}F-SMBT-1 binding were strongly associated ($R^2 > 0.94$), suggesting that a simplified tissue-ratio approach could be used to generate outcome measures. **Conclusion:** ^{18}F-SMBT-1 is a highly selective MAO-B tracer, with low nonspecific binding, high entry into the brain, and reversible kinetics. Moreover, ^{18}F-SMBT-1 brain distribution matches the reported in vitro distribution and captures the known MAO-B increases with age, suggesting that ^{18}F-SMBT-1 can potentially be used as a surrogate marker of reactive astrogliosis. Further validation of these findings with ^{18}F-SMBT-1 will require examination of a much larger series, including participants with mild cognitive impairment and AD.

Key Words: reactive astrogliosis; MAO-B; Alzheimer disease; amyloid; brain imaging

The neuropathologic hallmarks of Alzheimer disease (AD)—neurofibrillary tangles of tau protein and amyloid-β (Aβ) plaques—are accompanied by reactive gliosis, cellular degeneration, and diffuse synaptic and neuronal loss (1).

In recent years, there has been increased interest in the study of astrocytes (2). Astrocytes are the most abundant glial cells in the brain and are involved in several functions critical for the normal functioning and preservation of brain homeostasis (3,4), such as synaptic plasticity and formation of memory (5,6), regulation of γ-aminobutyric acid and glutamatergic neurotransmission (7–9), regulation of cerebral blood flow (10,11), and both Aβ production (12) and Aβ clearance (13). Astrocytes are also essential components of the neuroglial vascular unit, where they play a key neuroprotective role in cerebrovascular disease (10,11). Astrocytes do not constitute a homogeneous population and have been morphologically classified into protoplasmic, fibrous, and interlaminar or by their state: resting or activated (14). Although reactive astrocytes have also been classified as neurotoxic (A1), characterized by the expression of complement fraction 3, and neuroprotective (A2), expressing the S100A10 protein (15,16), reactive astrogliosis constitutes a much more complex spectrum of toxic and protective pathways (2,17), playing a crucial role in the pathophysiology of AD (9,18). Astrogliosis is an early neuroinflammatory event in several neurodegenerative conditions (19) such as AD (7,9,18), making it a target for the in vivo assessment of neuroinflammatory processes and their potential synergistic or independent contribution to the

development of AD dementia. In AD, reactive astrogliosis and microgliosis have been observed around both dense-core Aβ plaques and neurofibrillary tangles, and they are believed to contribute greatly to neurodegeneration throughout the course of the disease (18,20). In contrast to microgliosis, which is not detected by imaging at early disease stages (21), reactive astrogliosis occurs early (22), making it a particularly attractive target for understanding its contribution to AD pathogenesis and the development of dementia and, as such, is a potential therapeutic target for AD (23).

Reactive astrocytes overexpress monoamine oxidase B (MAO-B) (24), and molecular neuroimaging studies have used MAO-B tracers such as ^{11}C-L-deprenyl-D$_2$ (^{11}C-DED) as surrogate markers of astrogliosis (22,25–28). Some of these studies have shown that reactive astrogliosis is observed at the prodromal stages in both sporadic and familial AD (22,25). Historically, ^{11}C-DED has been used as a surrogate PET tracer for reactive astrogliosis; however, several issues limit the use of ^{11}C-DED, such as difficulty with quantification due to its irreversible kinetics, the existence of radiolabeled metabolites that can cross the blood–brain barrier and bind to monoamine transporters, poor image quality, and low selectivity for MAO-B (29). More recently another MAO-B tracer, ^{11}C-SL25.1188, with more favorable tracer kinetics than ^{11}C-DED was developed (30,31). ^{11}C-BU99008, a tracer for the imidazoline 2 binding sites, has also been proposed as a surrogate marker of astrogliosis (32–35). Unfortunately, like ^{11}C-DED, these tracers are labeled with ^{11}C, which has a 20-min half-life, preventing widespread clinical or research applications.

Recently, an analog of the PET radiotracer ^{18}F-THK5351, which was developed as a putative tau imaging radiotracer (36) but was later shown to have significant MAO-B binding (37,38), has been found to be highly selective for MAO-B (39). Preclinical assessment showed that ^{18}F-(S)-(2-methylpyrid-5-yl)-6-[(3-fluoro-2-hydroxy)propoxy]quinoline (^{18}F-SMBT-1) binds with high affinity (dissociation constant, 3.5 nM) and selectivity to MAO-B in human brain homogenates (39). Comparison of in vitro ^{18}F-SMBT-1 binding against MAO-B regional activity expressed as relative luminescence showed ^{18}F-SMBT-1 binding to correlate strongly with regional activity of MAO-B in the brain (39). Autoradiography studies showed significantly higher specific binding in the frontal cortex of an AD patient than in a control subject (39). Specific binding of ^{18}F-SMBT-1 was completely displaced after incubation with 1 μM of the selective MAO-B inhibitor lazabemide (39), showing high selectivity and low nonspecific binding. Receptor-binding screening assays showed no significant ^{18}F-SMBT-1 binding to 60 common neurotransmitter receptors, ion channels, and transporters (39). Radiation exposure was extrapolated to be 21.3 μSv/MBq for women and 12.2 μSv/MBq for men (39). Toxicity studies of ^{18}F-SMBT-1 in animals, including acute pharmacology and toxicity at doses 1,000–10,000 times higher than those expected in a PET study, demonstrated no toxic effects related to the drug treatment.

The aim of this first-in-humans study was to characterize ^{18}F-SMBT-1 binding, assessing its relation to age, regional brain distribution, and selectivity for MAO-B. We also examined ^{18}F-SMBT-1 tracer kinetics and explored potential quantification approaches.

MATERIALS AND METHODS

Participants

In total, 77 nonsmoking participants—53 who were elderly and cognitively normal (CN), 7 with mild cognitive impairment (MCI), 7 with AD, and 10 young and CN (YCN)—were recruited for the different aspects of the study. All participants were screened for unstable medical or psychiatric disease and concomitant medication. Participants with known use of antidepressants, cold and flu tablets, or opiate or opioid agonist medication were excluded because of the possibility of interactions with selegiline. For participants with a recognized memory impairment, this information was collected from a next of kin or caregiver. The study protocol was approved by the Austin Health Human Research Ethics Committee, and all participants gave written informed consent.

Image Acquisition

PET scans were acquired on 1 of 2 scanners, a Philips TF64 PET/CT or a Siemens Biograph mCT. A low-dose CT scan was obtained for attenuation correction. Partial-volume correction was not performed in any of the studies.

^{18}F-SMBT-1 PET. ^{18}F-SMBT-1 was synthesized in-house in the Department of Molecular Imaging and Therapy, Austin Health, using an ORA Neptis radiosynthesiser. The ^{18}F-SMBT-1 synthesis is detailed in the supplemental materials (available at http://jnm.snmjournals.org). Sixty-nine adults (10 YCN, 49 CN, 6 MCI, and 4 AD) participated in the assessment of ^{18}F-SMBT-1. All were administered 186 ± 6 MBq (range, 177–194 MBq). The average administered mass was 1.0 ± 0.8 μg (range 0.10–2.60 μg). Of the 69, 10 nondemented participants (4 CN and 6 MCI) underwent a 90-min dynamic scan after an intravenous bolus injection of ^{18}F-SMBT-1. The remaining 59 participants (10 YCN, 45 CN, and 4 AD) underwent a 20-min emission scan (4 × 5 min) starting at 60 min after injection of ^{18}F-SMBT-1. A second ^{18}F-SMBT-1 PET scan was acquired for 9 participants (5 CN and 4 AD) after completion of a 5-d regimen of oral selegiline.

Aβ PET. All 67 older adults underwent Aβ PET imaging with ^{18}F-flutemetamol (n = 3), ^{18}F-florbetapir (n = 2), or ^{18}F-NAV4694 (n = 62) to ascertain Aβ status. ^{18}F-NAV4694 and ^{18}F-florbetapir were synthesized in-house in the Department of Molecular Imaging and Therapy, Austin Health, as previously reported (40–42). ^{18}F-flutemetamol was manufactured by Cyclotek Pty Ltd. The ^{18}F-NAV4694 and ^{18}F-florbetapir PET acquisitions consisted of 20-min (4 × 5 min) dynamic scans obtained at 50 min after an intravenous bolus injection of 185 MBq (±10%) of ^{18}F-NAV4694 or ^{18}F-florbetapir. Similarly, the participants who received ^{18}F-flutemetamol also underwent a 20-min (4 × 5 min) PET acquisition starting at 90 min after injection of 185 MBq (±10%) of ^{18}F-flutemetamol. All Aβ imaging results were expressed in centiloids (40,41,43,44).

Tau PET. Nine older adults who were enrolled in the selegiline assessments with ^{18}F-SMBT-1 also underwent tau imaging with either 6-(fluoro-^{18}F)-3-(^{1}H-pyr- rolo[2,3-C]pyridin-1-yl)isoquinolin-5-amine (^{18}F-MK-6240) (n = 7) (45) or ^{18}F-PI2620 (n = 2) (46). Both tau imaging tracers were synthesized in-house in the Department of Molecular Imaging and Therapy, Austin Health, as previously reported (47). The ^{18}F-MK6240 PET acquisition consisted of a 20-min (4 × 5 min) dynamic scan acquired at 90 min after an intravenous bolus injection of 185 MBq (±10%) of ^{18}F-MK6240. The ^{18}F-PI2620 PET acquisition consisted of a 20-min (4 × 5 min) dynamic scan acquired at 80 min after an intravenous bolus injection of 200 MBq (±10%) of ^{18}F-PI2620. All tau imaging results were expressed as SUV ratios (SUVRs) using the cerebellar cortex as a reference region.

^{18}F-THK5351 PET. Eight older adults (4 CN, 1 MCI, and 3 AD) underwent 2 ^{18}F-THK5351 PET scans. ^{18}F-THK5351 was synthesized in-house in the Department of Molecular Imaging and Therapy, Austin Health, as previously described (48). Participants received an intravenous bolus injection of 185 MBq (±10%) of ^{18}F-THK5351, and a 30-min emission scan (4 × 5 min) was acquired starting at 50 min after injection. A second ^{18}F-THK5351 PET scan was acquired after completion of a 5-d regimen of oral selegiline.

MRI. Participants were also asked to undergo structural MRI on a 3-T TIM Trio scanner (Siemens Medical Solutions) to obtain

high-resolution T1-weighted anatomic magnetization-prepared rapid gradient-echo sequences.

Image Analysis

Aβ and tau PET scans were spatially normalized using CapAIBL (*44*). The standard centiloid method was applied to determine Aβ burden (*43*). A centiloid value of more than 20 was selected to determine a high-Aβ (Aβ+) scan (*49*). A 1.19 SUVR in the temporal composite region (*50*) was used to discriminate between high tau (tau-positive) and low tau (tau-negative). ^{18}F-THK5351 scans were spatially normalized using CapAIBL and expressed as SUVs. ^{18}F-SMBT-1 PET images were also spatially normalized using CapAIBL. ^{18}F-SMBT-1 PET volumes of interest were sampled to assess tracer selectivity, regional distribution, effect of age, and kinetic analysis. SUV values for the selegiline studies were estimated in 4 composite gray matter volumes of interest: neocortex (comprising frontal cortex, superior parietal lobe, lateral temporal lobe, lateral occipital lobe, anterior and posterior cingulate gyri, and precuneus), mesial temporal lobe (comprising hippocampus, entorhinal cortex, parahippocampus, and amygdala), basal ganglia (comprising caudate nuclei, putamen, globus pallidus, and thalamus), and cerebellar cortex. Several brain regions were evaluated as potential reference tissue, before generation of semiquantitative tissue ratios/SUVRs and graphical analysis of the data. Kinetic analysis was performed using PMOD (PMOD Technologies).

Assessing Tracer Selectivity Using Selegiline

Seventeen volunteers participated in the selegiline study. After a baseline ^{18}F-THK5351 or ^{18}F-SMBT-1 PET scan, the participants were supplied with oral selegiline tablets and instructed to follow a 5-d regimen at the standard therapeutic dose of 10 mg daily (5 mg at breakfast and 5 mg at lunch). At the completion of the regimen, the participants were invited back for a repeat PET scan.

Statistical Analysis

All statistical analyses were performed with JMP Pro (version 16.0; SAS Institute Inc.) for Macintosh (Apple). Data are presented as mean ± SD unless otherwise stated. Groups were compared using paired or unpaired Student t tests. Effect size was measured with Cohen d. Correlations were assessed by Spearman and Pearson correlation coefficients. Changes in tracer retention between pre- and postselegiline ^{18}F-THK5351 studies were expressed as percentage reduction from baseline. Significance was set at a P value of less than 0.05, uncorrected for multiple comparisons.

RESULTS

No significant changes in vital signs or in immediate or delayed adverse events related to the study drug were observed or reported by any of the participants during or after the ^{18}F-SMBT-1 scan.

Tracer Selectivity Studies

The irreversible MAO-B inhibitor selegiline was used to evaluate the selectivity of ^{18}F-SMBT. All participants underwent an Aβ and tau imaging scan, in addition to the 2 ^{18}F-SMBT-1 scans before and after selegiline. The same study was repeated with a different cohort of participants using ^{18}F-THK5351 to assess the validity of the selegiline regimen.

Table 1 shows the demographics of both groups. Tracer selectivity was assessed in 17 participants; 8 of them (4 CN, 3 Aβ+ AD, and 1 Aβ+ MCI) underwent assessment with ^{18}F-THK5351, whereas 9 (5 CN and 4 Aβ+ AD) underwent assessment with ^{18}F-SMBT-1.

For the selectivity study with ^{18}F-THK5351, 8 participants underwent Aβ PET and 2 ^{18}F-THK5351 PET scans, one at baseline and one after a 5-d regimen of 5 mg of oral selegiline twice daily. Figure 1A shows Aβ imaging studies performed with ^{18}F-flutemetamol in a CN subject and with ^{18}F-NAV4694 in an AD patient, as well as baseline ^{18}F-THK5351 PET images of the same individuals before and after the selegiline regimen, indicating a variable degree of blockade of the ^{18}F-THK5351. Given that there is a significant reduction in tracer retention in the cerebellar cortex, usually used as a reference region, all images are displayed in SUV units. Importantly, there is residual neocortical signal in the follow-up scan of the Aβ+ AD patient that is likely attributable to tau. Figure 1B shows a variable decrease in baseline ^{18}F-THK5351 signal in the neocortex (~63% decrease), mesial temporal lobe (~71% decrease), basal ganglia (~82% decrease), and cerebellar cortex (~54% decrease), although there were no significant differences in the degree of signal reduction between CN and AD subjects.

For the selectivity study with ^{18}F-SMBT-1, 9 participants (5 CN and 4 Aβ+ tau-positive AD) underwent Aβ and tau imaging and

TABLE 1
Demographics of ^{18}F-THK5351 and ^{18}F-SMBT-1 Selectivity Evaluations

Demographic	^{18}F-THK5351		^{18}F-SMBT-1	
	CN	AD/MCI	CN	AD
Total subjects (*n*)	4	4	5	4
Age (y)	79.1 ± 6.7	74.9 ± 7.0	78.5 ± 6.0	76.7 ± 1.5
Sex (*n*)	3 M/1 F	2 M/2 F	2 M/3 F	1 M/3 F
APOE4	25%	50%	60%	67%
MMSE	29.3 ± 0.5	25.7 ± 2.8*	29.2 ± 0.8	22.8 ± 4.8*
CDR SoB	0.0 ± 0.0	2.2 ± 0.4*	0.0 ± 0.0	7.6 ± 2.1*
Aβ (centiloids)	28.3 ± 54.7	82.7 ± 12.7	17.4 ± 10.2	127.6 ± 47.1
Aβ+	25%	100%	60%	100%

*Statistically significant ($P < 0.05$).
MMSE = Mini Mental State Examination; CDR SoB = clinical dementia rating sum of boxes.
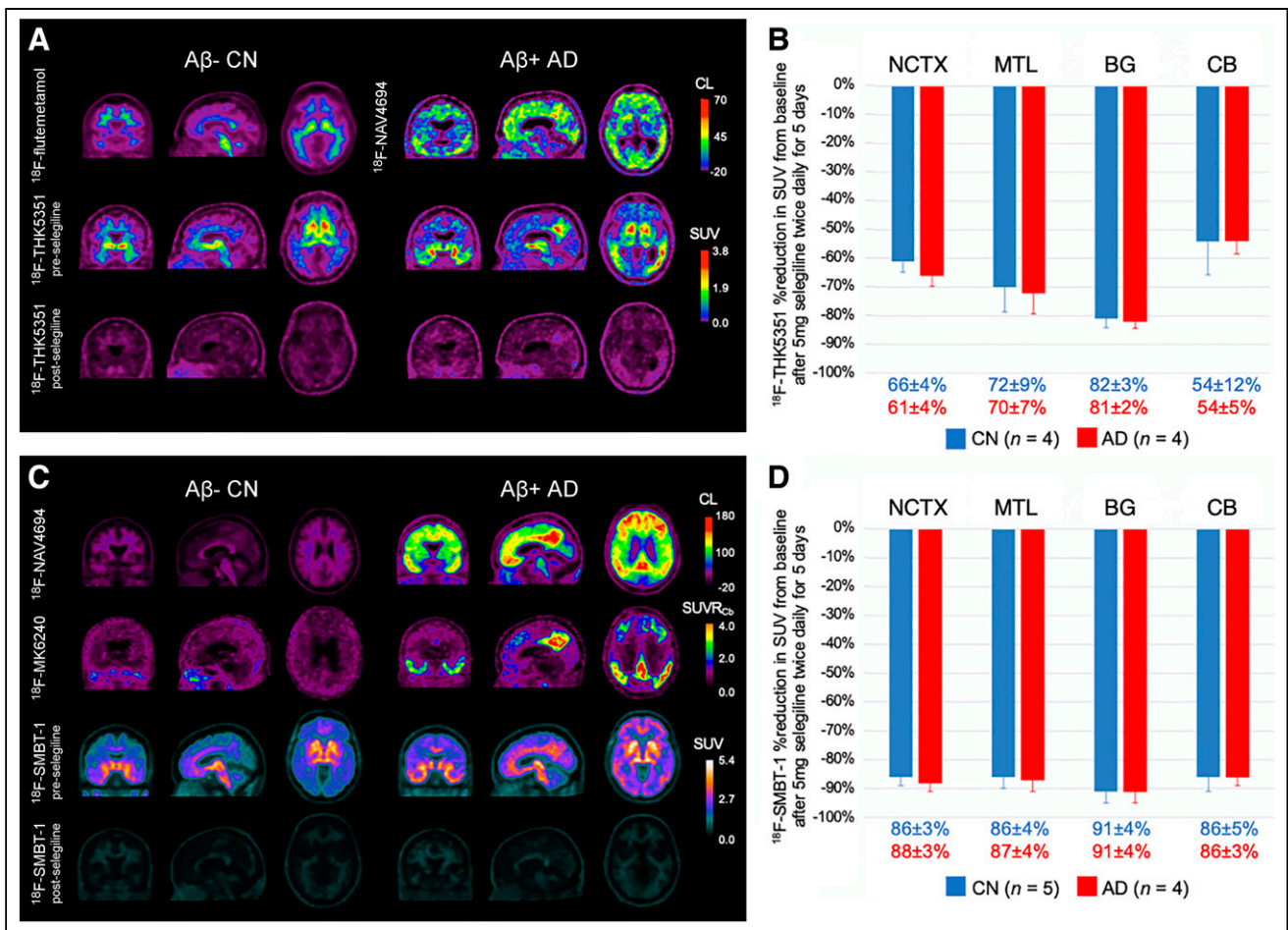Continuous data are mean ± SD.

FIGURE 1. Effect of selegiline on ^{18}F-THK5351 and ^{18}F-SMBT-1. (A) Representative coronal, sagittal, and transaxial PET images in Aβ-negative CN subject (79-y-old man; MMSE, 29) and in Aβ+ AD subject (72-y-old man; MMSE, 24). Aβ imaging studies are expressed in centiloids (top row) and were performed with ^{18}F-flutemetamol or ^{18}F-NAV4694. Baseline ^{18}F-THK5351 PET images (middle row) of same individuals before and after (bottom row) selegiline regimen indicate variable degree of regional blockade of ^{18}F-THK5351, most noticeable in basal ganglia, mesial temporal lobe, and neocortex. Given that there is significant reduction in tracer retention in cerebellar cortex, images are displayed in SUV units. Although in CN participants there is significant reduction of ^{18}F-THK5351 retention throughout brain, in AD patients there is residual cortical retention likely due to ^{18}F-THK5351 binding to tau. (B) Bar graphs showing percentage of selegiline ^{18}F-THK5351 regional blockade in neocortex (∼63% decrease), mesial temporal lobe (∼71% decrease), basal ganglia (∼82% decrease), and cerebellum (∼54% decrease). Reduction of signal was greater in basal ganglia and mesial temporal lobe than in neocortex and cerebellum, although there were no significant differences in degree of signal reduction between CN and AD subjects. (C) Representative coronal, sagittal, and transaxial PET images in Aβ-negative, tau-negative CN subject (78-y-old woman; MMSE, 29) and in Aβ+, tau-positive AD subjects (75-y-old woman; MMSE, 21). Aβ imaging studies performed with ^{18}F-NAV4694 are expressed in centiloids (top row). Second row shows tau imaging studies expressed in SUVR using cerebellar cortex as reference region, performed with either ^{18}F-MK6240 or ^{18}F-PI2620. Baseline ^{18}F-SMBT-1 PET images (third row) of same individuals before and after (bottom row) selegiline regimen indicate high degree of regional blockade of ^{18}F-SMBT-1 across all regions of brain. Images are displayed in SUV units. In contrast to ^{18}F-THK5351 (Fig. 1A), there was no residual cortical retention in CN or AD subjects. (D) Bar graphs showing high percentage of blocking of ^{18}F-SMBT-1 by selegiline, with more than 85% blockade across all regions of brain, indicating selective binding of ^{18}F-SMBT-1 to MAO-B as well as low nonspecific binding. There were no significant differences in degree of signal reduction between regions or between CN and AD subjects. BG = basal ganglia; CB = cerebellum; CL = centiloids; MTL = mesial temporal lobe; NCTX = neocortex.

2 ^{18}F-SMBT-1 PET scans, one at baseline and one after the same 5-d regimen of 5 mg of oral selegiline twice daily. Figure 1C shows Aβ imaging studies with ^{18}F-NAV4694 and tau imaging studies with ^{18}F-MK6240, using the cerebellar cortex as a reference region, in a CN subject and an AD subject. The ^{18}F-SMBT-1 SUV images before and after the selegiline regimen indicate a very high degree of reduction in ^{18}F-SMBT-1 signal, with no residual activity attributable to Aβ or tau. Figure 1D shows a more than 85% decrease in baseline ^{18}F-SMBT-1 signal in the neocortex, mesial temporal lobe, basal ganglia, and cerebellum, with the same degree of signal reduction in CN and AD subjects. A more detailed brain regional blockade by selegiline is provided in Table 2.

Regional Brain Distribution of ^{18}F-SMBT-1

We also assessed the in vivo regional brain distribution of ^{18}F-SMBT-1. Figure 2 shows ^{18}F-SMBT-1 SUV at 60–80 min after injection in 44 low-Aβ (Aβ-negative) CN subjects, against the reported in vitro ^{11}C-DED autoradiography regional concentrations (51). There was a strong correlation ($R^2 = 0.84$, $P = 0.0002$) between the in vivo regional ^{18}F-SMBT-1 signal and the in vitro concentrations in several regions of the brain.

Increase in MAO-B with Age

To further evaluate ^{18}F-SMBT-1, we scanned 10 YCN subjects (5 women, 5 men; 31.3 ± 4.0 y old) (Table 3) to assess whether

TABLE 2
Percentage Reduction in Regional ^{18}F-THK5351 and ^{18}F-SMBT-1 SUV by Selegiline

Region	^{18}F-THK-5351		^{18}F-SMBT-1	
	CN	AD	CN	AD
Caudate	−86%	−84%	93%	95%
Thalamus	−83%	−82%	93%	95%
Putamen	−80%	−78%	92%	92%
Anterior cingulate	−76%	−74%	88%	90%
Hippocampus	−69%	−64%	88%	90%
Frontal cortex	−67%	−63%	87%	89%
Temporal	−67%	−67%	87%	88%
Posterior cingulate	−66%	−63%	86%	88%
Parietal	−63%	−56%	85%	86%
Cerebellar cortex	−54%	−54%	86%	86%
Whole cerebellum	−72%	−68%	83%	83%
Pons	−73%	−68%	82%	82%
Midbrain	−66%	−63%	82%	81%
Occipital	−61%	−56%	80%	83%
Cerebellar white matter	−65%	−56%	69%	69%
SWM + corpus callosum	−64%	−57%	62%	65%
SWM	−54%	−54%	60%	63%

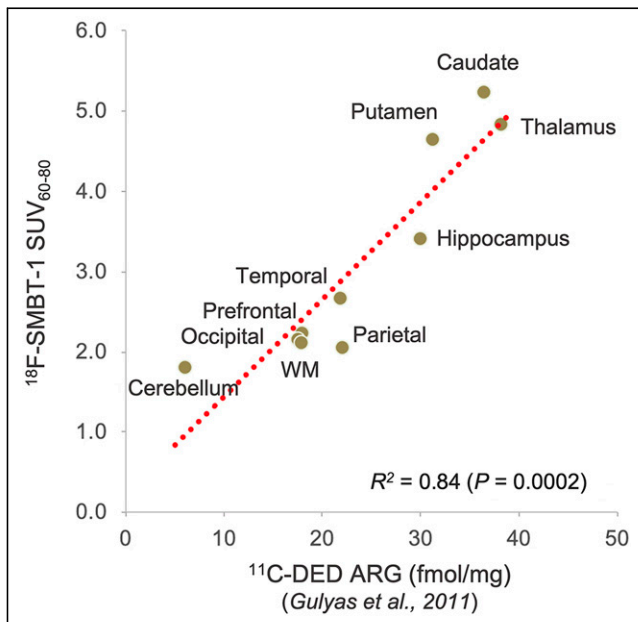No P values were statistically significant for CN ≠ AD.

FIGURE 2. Regional distribution of MAO-B in brain: correlation between in vitro autoradiography with ^{11}C-DED and ^{18}F-SMBT-1 retention in Aβ-negative CN subjects. There was high correlation (R^2 = 0.84) between known in vitro regional distribution of MAO-B in brain (51), expressed in fmol/mg, and regional SMBT-1 retention at 60–80 min after injection. ARG = autoradiography; WM = white matter.

^{18}F-SMBT-1 was able to capture the age-related increases of MAO-B in the frontal cortex as previously reported by in vitro studies (52). ^{18}F-SMBT-1 SUV in the frontal cortex of 10 YCN and 44 Aβ-negative tau-negative CN subjects (Fig. 3A) demonstrated a significant age-related increase in MAO-B (R^2 = 0.44, P < 0.0001). Figure 3B shows coronal, sagittal, and transaxial

TABLE 3
Demographics for Assessment of Effect of Age

Demographic	YCN	Aβ-negative CN
Total subjects (n)	10	44
Age (y)	31.3 ± 4.0*	76.0 ± 4.8
Female	50%	57%
Education (y)		14.8 ± 2.7
APOE4		30%
MMSE		28.6 ± 1.5
CDR SoB		0.07 ± 0.2
Aβ burden (centiloids)		0.80 ± 6.9

*Statistically significant association (P < 0.05).
MMSE = Mini Mental State Examination; CDR SoB = clinical dementia rating sum of boxes.
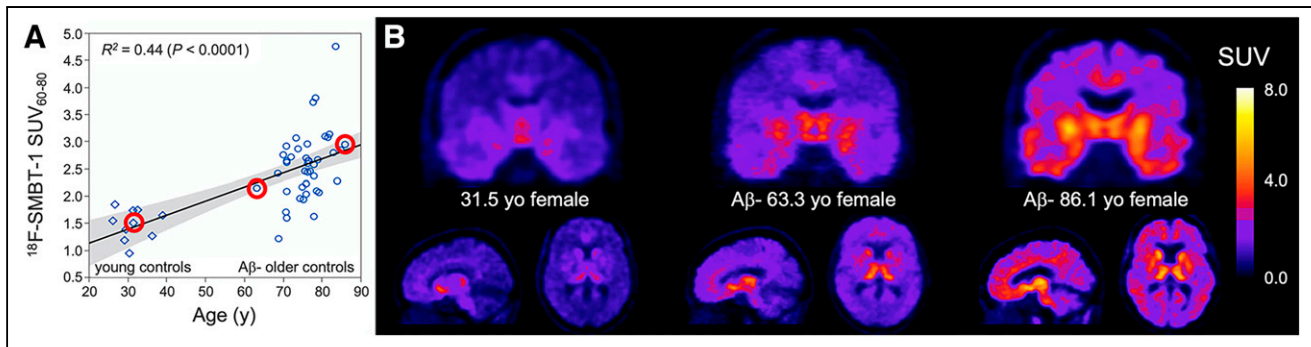
FIGURE 3. Effect of age. (A) ^{18}F-SMBT-1 SUV at 60–80 min after injection in frontal cortex of 10 YCN subjects (5 women, 5 men; 31.3 ± 4.0 y old) and 44 Aβ-negative CN subjects (25 women, 19 men; 76.0 ± 4.8 y old) was able to capture reported age-related increases of MAO-B in frontal cortex as previously reported by in vitro studies (52) and in vivo with PET (62). (B) Coronal, sagittal, and transaxial ^{18}F-SMBT-1 images illustrating age-related regional increases in ^{18}F-SMBT-1 signal in 3 women, whose ages ranged from 31 to 86 y (red circles in A).

images illustrating the age-related regional increases in ^{18}F-SMBT-1 signal in 3 women, whose ages ranged from 31 to 86 y old.

^{18}F-SMBT-1 Kinetics

We characterized the in vivo ^{18}F-SMBT-1 kinetics in 10 elderly participants (6 MCI and 4 CN, Table 4). Time–activity curves revealed that ^{18}F-SMBT-1 has robust entry into the brain (SUV, 4–7 at ∼3–5 min after injection) and displays reversible kinetics (Fig. 4A). ^{18}F-SMBT-1 retention was highest in the basal ganglia and thalamus; intermediate in the anterior cingulate, gyrus rectus, and hippocampus; low in neocortical areas; and lowest in the cerebellum and in the subcortical white matter (SWM).

Before generating SUVRs over time, we compared the SUVs in several potential reference regions—cerebellum, cerebellar white matter, SWM (53), SWM, and corpus callosum (54)—to be used in a simplified reference tissue model (55). The SUVR generated with the SWM as a reference region had the strongest correlation with the in vitro regional distribution of MAO-B (Table 5) (51).

SUVRs were shown to approach an apparent steady state in high-binding areas approximately 50 min after injection (Fig. 4B), suggesting the possibility of using a simplified ^{18}F-SMBT-1 imaging protocol with SUVR as the outcome. ^{18}F-SMBT-1 reversible kinetics were further validated by graphical analysis of the 90-min dynamic scans, using the same regions as used for generating SUVRs. ^{18}F-SMBT-1 specific binding measures of distribution volume derived

TABLE 4
Demographics for Assessing ^{18}F-SMBT-1 Tracer Kinetics

Demographic	CN/MCI
Total subjects (n)	10
Age (y)	73.2 ± 7.2
Female	30%
APOE4	60%
MMSE	27.7 ± 1.6
CDR SoB	0.3 ± 0.4
Aβ burden (centiloids)	15.8 ± 31.0
Aβ+	30%

MMSE = Mini Mental State Examination; CDR SoB = clinical dementia rating sum of boxes.

from the noninvasive Logan plot (56), as well as nondisplaceable binding potential estimated using the Ichise multilinear reference tissue model, MRTM (57), showed high correlations with late-scan SUVR ($R^2 = 0.97$ and 0.94 for nondisplaceable binding potential and distribution volume, respectively) and with the known distribution of MAO-B in the human brain ($R^2 = 0.78$ and 0.72 for nondisplaceable binding potential and distribution volume, respectively) (51).

DISCUSSION

To the best of our knowledge, ^{18}F-SMBT-1 represents the first available ^{18}F MAO-B radiotracer to be used in a clinical study. Because preclinical evaluation demonstrated ^{18}F-SMBT-1 to have an in vitro binding profile well suited for an MAO-B PET tracer (39), the study aimed at characterizing the ^{18}F-SMBT-1 binding profile in vivo with PET. The study was divided into 4 main areas or substudies. We first assessed ^{18}F-SMBT-1 selectivity for MAO-B before and after a 5-d regimen of oral selegiline. ^{18}F-SMBT-1 is an analog of the PET radiotracer ^{18}F-THK5351, which was developed as a putative tau imaging radiotracer (39) but was later shown to have significant MAO-B binding (37,38). Therefore, we compared the ^{18}F-SMBT-1 results with studies performed with ^{18}F-THK5351 under the same selegiline regimen. For these studies, given that there is a significant widespread reduction in tracer retention even in regions usually used as an internal reference, all images were displayed in SUV units. In the ^{18}F-THK5351 studies, the degree of blockade by selegiline in gray matter areas was variable, ranging from 54% in the cerebellar cortex to more than 80% in the basal ganglia. Moreover, there was some residual ^{18}F-THK5351 signal in the cortex, likely representing ^{18}F-THK5351 binding to tau. In the ^{18}F-SMBT-1 studies, the degree of blockade by selegiline in gray matter areas was more than 85%, and most importantly, there was no residual cortical signal. There were no significant differences in the degree of signal reduction between CN and AD subjects with either ^{18}F-THK5351 or ^{18}F-SMBT-1. This study also demonstrated the low degree of nonspecific binding with ^{18}F-SMBT-1. This is important because it enables ^{18}F-SMBT-1 to accurately detect incipient early cortical changes in MAO-B concentrations as well as small changes over time. The low nonspecific binding is also evident in the high-contrast images (Fig. 1C) even at 60–80 min after injection. We then assessed the regional brain distribution of ^{18}F-SMBT-1 and compared the results with in vitro autoradiography performed with ^{11}C-DED (51), showing a high correlation between the two.
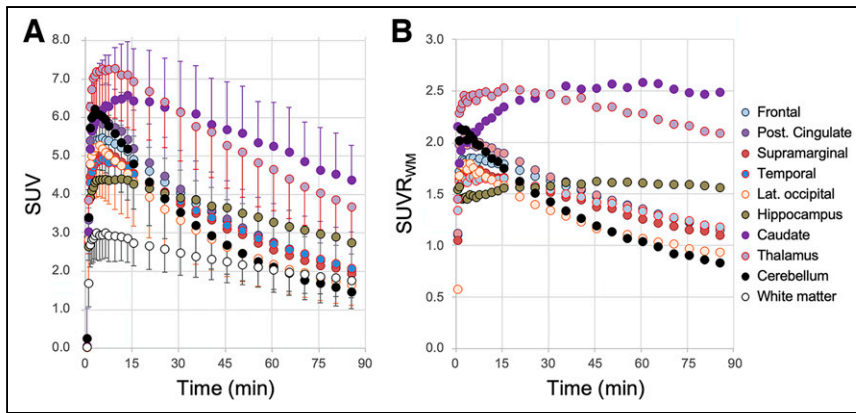
FIGURE 4. ^{18}F-SMBT-1 time–activity and total binding curves. (A) Time–activity curves reveal that ^{18}F-SMBT-1 has robust entry into brain (SUV, 5–7 at ~5 min after injection) and reversible kinetics. ^{18}F-SMBT-1 clearance was slower in areas of high concentrations of MAO-B, such as basal ganglia and hippocampus, and faster in regions with lower MAO-B concentrations, such as frontal cortex, temporal lobe, and cerebellum. (B) Tissue ratios—using SWM as reference region—over time show SWM SUVR approaching apparent steady state in high binding areas ~50 min after injection. SWM was more stable reference region across clinical groups and across Aβ status.

The competition studies with selegiline and the regional distribution studies indicate that ^{18}F-SMBT-1 is a highly selective ^{18}F-labeled MAO-B tracer (7).

^{18}F-SMBT-1 was also able to capture the known increases in MAO-B with age. The estimated yearly signal increase for ^{18}F-SMBT-1 in the frontal cortex is about 2.5%/y, similar to the approximately 1.9%/y estimates from in vitro studies (52).

Finally, we evaluated the tracer kinetic characteristics of ^{18}F-SMBT-1. The time–activity curves showed high initial entry into the brain, followed by clearance of the tracer. Clearance was slower in areas with very high MAO-B concentrations such as

TABLE 5
Correlation Between MAO-B In Vitro Distribution and ^{18}F-SMBT-1 Binding Parameters and Tissue Ratios Generated with Different Reference Regions

Parameter	r	95% CI	P
SWM SUVR	0.914	0.62–0.98	0.0002
SUVR	0.904	0.61–0.98	0.0007
Cerebellum			
SWM + corpus callosum	0.889	0.55–0.98	0.0013
Cerebellar white matter	0.888	0.55–0.98	0.0014
Ichise nondisplaceable binding potential	0.885	0.54–0.98	0.0015
Logan total distribution volume ratio	0.849	0.42–0.97	0.0038

Correlation between in vitro MAO-B brain distribution assessed with autoradiography (51) and quantitative and semiquantitative measures of ^{18}F-SMBT-1 binding, ranked by correlation coefficients (r). Tissue ratios and graphical analysis results using SWM as reference region yielded highest correlation with in vitro measures of MAO-B.

the basal ganglia, intermediate in areas with high MAO-B concentrations such as the hippocampus and anterior cingulate gyrus, and faster in cortical areas with low concentrations of MAO-B such as the neocortical areas. The lowest retention was observed in SWM. The reversible binding kinetics suggested that ^{18}F-SMBT-1 binding could be quantified using graphical analysis (56,57) and a simplified reference tissue model (55).

Before embarking on the generation of tissue ratios and graphical analysis of the data, we explored several potential reference regions. We correlated the tissue ratios generated with each of them against the known regional distribution of MAO-B in the brain. SWM SUVR yielded the strongest correlation. Moreover, the SWM was the region least affected by selegiline (Table 2) and one of the least atrophic regions across the AD continuum (58). Graphical analysis outcomes, either multilinear reference tissue model or Logan plot, also generated using the SWM as reference region, correlated strongly with SWM SUVR and with the in vitro brain distribution of MAO-B. The small number of MCI and AD patients precludes drawing any conclusion regarding group differences in the ^{18}F-SMBT-1 signal. A larger sample size of MCI and AD patients, with their corresponding Aβ and tau status, will be required to examine whether ^{18}F-SMBT-1 can capture the reported increases in MAO-B in AD.

Although most of the recently developed specific neuroimaging and biofluid markers of disease have focused on the pathologic hallmarks of AD, such as Aβ plaques and tau tangles, the most prevalent markers identified in genomewide association studies of AD are related to neuroinflammation (59). The introduction of biomarker-based approaches to identifying brain pathology has informed new strategies for the design of preventative clinical trials aimed at preventing the onset of cognitive impairment and dementia. Markers of Aβ and tau pathology and markers of neurodegeneration have been incorporated into a recently proposed biomarker-based framework (60). In view of the advantage of the modular design of the framework, and considering that reactive gliosis is a critical aspect of the neuropathology of AD, the biomarker framework might be expanded to include reactive gliosis.

There are several limitations to the study. There is no validation of the semiquantitative or simplified reference region approach by full kinetic analysis with metabolite-corrected arterial input function. The same applies to the selection of the reference region. Initial semiquantitative and quantitative examinations used the SWM as the reference region. Although SWM was affected significantly less by the selegiline regimen than were the cortical, subcortical, or cerebellar regions (~60% vs. >85% blockade), the selegiline study clearly indicates that there is substantial specific binding in SWM. This, in principle, would preclude the use of SWM as a reference region. It could be argued that SWM represents a brain region that is not likely to be involved in the early disease process; although there is SWM atrophy in AD, atrophy is more prevalent around mesial temporal lobe structures (58). Another issue to consider is that SWM, *stricto sensu*, does not truly fulfill the criteria for a reference region (55) given that it has a completely different cellular

composition, has about half the regional cerebral blood flow of gray matter, and is likely to have a completely different degree of nonspecific binding. A more appropriate term for it might be *internal brain scaling region*. The kinetic analysis was performed pooling CN and MCI subjects, with 30% being deemed Aβ+. Probably because of the small numbers, there were no significant kinetic differences between CN and MCI subjects, nor were there significant kinetic differences when comparing Aβ-negative with Aβ+.

CONCLUSION

Our first-in-humans studies confirmed that ^{18}F-SMBT-1 is a selective MAO-B tracer. Although the main goal was to characterize an MAO-B tracer to be used as a surrogate marker of astrogliosis in neurodegenerative conditions, the potential applications of an MAO-B tracer are much wider, extending from neuropsychiatric conditions such as depression (*30*) to movement disorders (*61*). In the particular case of assessing astrogliosis, ^{18}F-SMBT-1 will allow a better understanding of the pathophysiology of AD while examining its potential direct or indirect effect over neurodegeneration, cognitive decline, and clinical progression, enabling more accurate staging and prognosis at earlier stages of the disease.

DISCLOSURE

ACKNOWLEDGMENTS

KEY POINTS

QUESTION: Is ^{18}F-SMBT-1 a selective MAO-B tracer?

PERTINENT FINDINGS: A clinical study in 59 elderly and 10 young participants showed that ^{18}F-SMBT-1 is a highly selective MAO-B tracer, with reversible kinetics and low specific signal that follows the known regional distribution of MAO-B in the brain and captures the known increases in MAO-B with age.

IMPLICATIONS FOR PATIENT CARE: ^{18}F-SMBT-1 can be used as a surrogate marker of reactive astrogliosis

REFERENCES

1. Masters CL, Beyreuther K. The neuropathology of Alzheimer's disease in the year 2005. In: Beal MF, Lang AE, Ludolph AC, eds. *Neurodegenerative Diseases: Neurobiology, Pathogenesis and Therapeutics.* Cambridge University Press; 2005: 433–440.
2. Escartin C, Galea E, Lakatos A, et al. Reactive astrocyte nomenclature, definitions, and future directions. *Nat Neurosci.* 2021;24:312–325.
3. Fakhoury M. Microglia and astrocytes in Alzheimer's disease: implications for therapy. *Curr Neuropharmacol.* 2018;16:508–518.
4. Vasile F, Dossi E, Rouach N. Human astrocytes: structure and functions in the healthy brain. *Brain Struct Funct.* 2017;222:2017–2029.
5. Adamsky A, Kol A, Kreisel T, et al. Astrocytic activation generates de novo neuronal potentiation and memory enhancement. *Cell.* 2018;174:59–71 e14.
6. Kol A, Adamsky A, Groysman M, Kreisel T, London M, Goshen I. Astrocytes contribute to remote memory formation by modulating hippocampal-cortical communication during learning. *Nat Neurosci.* 2020;23:1229–1239.
7. Osborn LM, Kamphuis W, Wadman WJ, Hol EM. Astrogliosis: an integral player in the pathogenesis of Alzheimer's disease. *Prog Neurobiol.* 2016;144:121–141.
8. Danbolt NC, Furness DN, Zhou Y. Neuronal vs glial glutamate uptake: resolving the conundrum. *Neurochem Int.* 2016;98:29–45.
9. Carter SF, Herholz K, Rosa-Neto P, Pellerin L, Nordberg A, Zimmer ER. Astrocyte biomarkers in Alzheimer's disease. *Trends Mol Med.* 2019;25:77–95.
10. Iadecola C, Nedergaard M. Glial regulation of the cerebral microvasculature. *Nat Neurosci.* 2007;10:1369–1376.
11. Koehler RC, Roman RJ, Harder DR. Astrocytes and the regulation of cerebral blood flow. *Trends Neurosci.* 2009;32:160–169.
12. Zhao J, O'Connor T, Vassar R. The contribution of activated astrocytes to Abeta production: implications for Alzheimer's disease pathogenesis. *J Neuroinflammation.* 2011;8:150.
13. Thal DR. The role of astrocytes in amyloid beta-protein toxicity and clearance. *Exp Neurol.* 2012;236:1–5.
14. Perez-Nievas BG, Serrano-Pozo A. Deciphering the astrocyte reaction in Alzheimer's disease. *Front Aging Neurosci.* 2018;10:114.
15. Zamanian JL, Xu L, Foo LC, et al. Genomic analysis of reactive astrogliosis. *J Neurosci.* 2012;32:6391–6410.
16. Liddelow SA, Barres BA. Reactive astrocytes: production, function, and therapeutic potential. *Immunity.* 2017;46:957–967.
17. Sofroniew MV. Astrogliosis. *Cold Spring Harb Perspect Biol.* 2014;7:a020420.
18. Birch AM. The contribution of astrocytes to Alzheimer's disease. *Biochem Soc Trans.* 2014;42:1316–1320.
19. Acioglu C, Li L, Elkabes S. Contribution of astrocytes to neuropathology of neurodegenerative diseases. *Brain Res.* 2021;1758:147291.
20. Ingelsson M, Fukumoto H, Newell KL, et al. Early Abeta accumulation and progressive synaptic loss, gliosis, and tangle formation in AD brain. *Neurology.* 2004; 62:925–931.
21. Kreisl WC, Lyoo CH, Liow JS, et al. ^{11}C-PBR28 binding to translocator protein increases with progression of Alzheimer's disease. *Neurobiol Aging.* 2016; 44:53–61.
22. Carter SF, Scholl M, Almkvist O, et al. Evidence for astrocytosis in prodromal Alzheimer disease provided by ^{11}C-deuterium-L-deprenyl: a multitracer PET paradigm combining ^{11}C-Pittsburgh compound B and ^{18}F-FDG. *J Nucl Med.* 2012;53:37–46.
23. Assefa BT, Gebre AK, Altaye BM. Reactive astrocytes as drug target in Alzheimer's disease. *BioMed Res Int.* 2018;2018:4160247.
24. Ekblom J, Jossan SS, Bergstrom M, Oreland L, Walum E, Aquilonius SM. Monoamine oxidase-B in astrocytes. *Glia.* 1993;8:122–132.
25. Rodriguez-Vieitez E, Ni R, Gulyas B, et al. Astrocytosis precedes amyloid plaque deposition in Alzheimer APPswe transgenic mouse brain: a correlative positron emission tomography and in vitro imaging study. *Eur J Nucl Med Mol Imaging.* 2015;42:1119–1132.
26. Rodriguez-Vieitez E, Saint-Aubert L, Carter SF, et al. Diverging longitudinal changes in astrocytosis and amyloid PET in autosomal dominant Alzheimer's disease. *Brain.* 2016;139:922–936.
27. Schöll M, Carter SF, Westman E, et al. Early astrocytosis in autosomal dominant Alzheimer's disease measured in vivo by multi-tracer positron emission tomography. *Sci Rep.* 2015;5:16404.
28. Engler H, Nennesmo I, Kumlien E, et al. Imaging astrocytosis with PET in Creutzfeldt-Jakob disease: case report with histopathological findings. *Int J Clin Exp Med.* 2012;5:201–207.
29. Jevtić II, Lai TH, Penjišević JZ, et al. Newly synthesized fluorinated cinnamylpiperazines possessing low in vitro MAO-B binding. *Molecules.* 2020;25:4941.
30. Moriguchi S, Wilson AA, Miler L, et al. Monoamine oxidase B total distribution volume in the prefrontal cortex of major depressive disorder: an [^{11}C]SL25.1188 positron emission tomography study. *JAMA Psychiatry.* 2019;76:634–641.
31. Saba W, Valette H, Peyronneau MA, et al. [^{11}C]SL25.1188, a new reversible radioligand to study the monoamine oxidase type B with PET: preclinical characterisation in nonhuman primate. *Synapse.* 2010;64:61–69.
32. Tyacke RJ, Myers JFM, Venkataraman A, et al. Evaluation of ^{11}C-BU99008, a PET ligand for the imidazoline2 binding site in human brain. *J Nucl Med.* 2018;59: 1597–1602.

33. Venkataraman AV, Keat N, Myers JF, et al. First evaluation of PET-based human biodistribution and radiation dosimetry of ^{11}C-BU99008, a tracer for imaging the imidazoline2 binding site. *EJNMMI Res.* 2018;8:71.

34. Kumar A, Koistinen NA, Malarte ML, et al. Astroglial tracer BU99008 detects multiple binding sites in Alzheimer's disease brain. *Mol Psychiatry.* 2021;26:5833–5847.

35. Calsolaro V, Matthews PM, Donat CK, et al. Astrocyte reactivity with late-onset cognitive impairment assessed in vivo using ^{11}C-BU99008 PET and its relationship with amyloid load. *Mol Psychiatry.* 2021;26:5848–5855.

36. Harada R, Okamura N, Furumoto S, et al. ^{18}F-THK5351: a novel PET radiotracer for imaging neurofibrillary pathology in Alzheimer disease. *J Nucl Med.* 2016;57:208–214.

37. Ng KP, Pascoal TA, Mathotaarachchi S, et al. Monoamine oxidase B inhibitor, seleginine, reduces ^{18}F-THK5351 uptake in the human brain. *Alzheimers Res Ther.* 2017;9:25.

38. Harada R, Ishiki A, Kai H, et al. Correlations of ^{18}F-THK5351 PET with postmortem burden of tau and astrogliosis in Alzheimer disease. *J Nucl Med.* 2018;59:671–674.

39. Harada R, Hayakawa Y, Ezura M, et al. ^{18}F-SMBT-1: a selective and reversible PET tracer for monoamine oxidase-B imaging. *J Nucl Med.* 2021;62:253–258.

40. Battle MR, Pillay LC, Lowe VJ, et al. Centiloid scaling for quantification of brain amyloid with [18F]flutemetamol using multiple processing methods. *EJNMMI Res.* 2018;8:107.

41. Rowe CC, Jones G, Dore V, et al. Standardized expression of ^{18}F-NAV4694 and ^{11}C-PiB beta-amyloid PET results with the centiloid scale. *J Nucl Med.* 2016;57: 1233–1237.

42. Navitsky M, Joshi AD, Kennedy I, et al. Standardization of amyloid quantitation with florbetapir standardized uptake value ratios to the centiloid scale. *Alzheimers Dement.* 2018;14:1565–1571.

43. Klunk WE, Koeppe RA, Price JC, et al. The centiloid project: standardizing quantitative amyloid plaque estimation by PET. *Alzheimers Dement.* 2015;11:1-15.e4.

44. Bourgeat P, Dore V, Fripp J, et al. Implementing the centiloid transformation for ^{11}C-PiB and beta-amyloid ^{18}F-PET tracers using CapAIBL. *Neuroimage.* 2018; 183:387–393.

45. Walji AM, Hostetler ED, Selnick H, et al. Discovery of 6-(fluoro-^{18}F)-3-([1]H-pyr-rolo[2,3-C]pyridin-1-yl)isoquinolin-5-amine (^{18}F-MK-6240): a positron emission tomography (PET) imaging agent for quantification of neurofibrillary tangles (NFTs). *J Med Chem.* 2016;59:4778–4789.

46. Brendel M, Barthel H, van Eimeren T, et al. Assessment of 18F-PI-2620 as a biomarker in progressive supranuclear palsy. *JAMA Neurol.* 2020;77:1408–1419.

47. Krishnadas N, Dore V, Lamb F, et al. Case report: ^{18}F-MK6240 tau positron emission tomography pattern resembling chronic traumatic encephalopathy in a retired Australian rules football player. *Front Neurol.* 2020;11:598980.

48. Ishiki A, Harada R, Okamura N, et al. Tau imaging with [18F]THK-5351 in progressive supranuclear palsy. *Eur J Neurol.* 2017;24:130–136.

49. Jack CR Jr, Wiste HJ, Weigand SD, et al. Defining imaging biomarker cut points for brain aging and Alzheimer's disease. *Alzheimers Dement.* 2017;13: 205–216.

50. Jack CR Jr, Wiste HJ, Schwarz CG, et al. Longitudinal tau PET in ageing and Alzheimer's disease. *Brain.* 2018;141:1517–1528.

51. Gulyás B, Pavlova E, Kasa P, et al. Activated MAO-B in the brain of Alzheimer patients, demonstrated by [^{11}C]-L-deprenyl using whole hemisphere autoradiography. *Neurochem Int.* 2011;58:60–68.

52. Galva MD, Bondiolotti GP, Olasmaa M, Picotti GB. Effect of aging on lazabemide binding, monoamine oxidase activity and monoamine metabolites in human frontal cortex. *J Neural Transm Gen Sect.* 1995;101:83–94.

53. Fleisher AS, Joshi AD, Sundell KL, et al. Use of white matter reference regions for detection of change in florbetapir positron emission tomography from completed phase 3 solanezumab trials. *Alzheimers Dement.* 2017;13:1117–1124.

54. Chen K, Roontiva A, Thiyyagura P, et al. Improved power for characterizing longitudinal amyloid-beta PET changes and evaluating amyloid-modifying treatments with a cerebral white matter reference region. *J Nucl Med.* 2015; 56:560–566.

55. Lammertsma AA, Hume SP. Simplified reference tissue model for PET receptor studies. *Neuroimage.* 1996;4:153–158.

56. Logan J, Fowler JS, Volkow ND, Wang GJ, Ding YS, Alexoff DL. Distribution volume ratios without blood sampling from graphical analysis of PET data. *J Cereb Blood Flow Metab.* 1996;16:834–840.

57. Ichise M, Ballinger JR, Golan H, et al. Noninvasive quantification of dopamine D2 receptors with iodine-123-IBF SPECT. *J Nucl Med.* 1996;37:513–520.

58. Li J, Pan P, Huang R, Shang H. A meta-analysis of voxel-based morphometry studies of white matter volume alterations in Alzheimer's disease. *Neurosci Biobehav Rev.* 2012;36:757–763.

59. Hammond TR, Marsh SE, Stevens B. Immune signaling in neurodegeneration. *Immunity.* 2019;50:955–974.

60. Jack CR Jr, Bennett DA, Blennow K, et al. A/T/N: an unbiased descriptive classification scheme for Alzheimer disease biomarkers. *Neurology.* 2016;87: 539–547.

61. Cohen G, Farooqui R, Kesler N. Parkinson disease: a new link between monoamine oxidase and mitochondrial electron flow. *Proc Natl Acad Sci USA.* 1997;94: 4890–4894.

62. Fowler JS, Volkow ND, Wang GJ, et al. Age-related increases in brain monoamine oxidase B in living healthy human subjects. *Neurobiol Aging.* 1997;18:431–435.